

Gradient bundle analysis of ketosteroid isomerase

Timothy R. Wilson,¹ Amanda Morgenstern,² Anastassia N. Alexandrova,³ and M.E. Eberhart^{1,a}

¹*Department of Chemistry, Colorado School of Mines*

²*Department of Chemistry & Biochemistry, UCCS*

³*Department of Chemistry, UCLA*

^a*Corresponding author. Email: meberhar@mines.edu*

May 20, 2022

Abstract

Bond bundle analysis is used to investigate enzymatic catalysis in the KSI active site. We identify the unique bonding regions in five KSI systems, including those exposed to applied oriented electric fields and those with amino acid mutations, and calculate the precise redistribution of electron density that accompanies either enhancement or inhibition of KSI catalytic activity. In two examples—using direct inspection of bond bundle regional properties, and using correlations between those properties and reaction barrier height—we arrive at similar conclusions, that catalytic enhancement results from promoting electron density redistribution between bonds within the KSI-docked substrate molecule in a way that closely resembles our mechanistic understanding of the forward catalyzed reaction. The catalyzing charge redistribution between bond bundles is prevalent in KSI systems catalyzed via electric fields or via amino acid mutation, and are thus suggestive of a general catalytic role.

Keywords: *bond bundle, bond wedge, gradient bundle analysis, gradient bundle decomposition, KSI, enzymatic catalysis, electron density analysis, QTAIM*

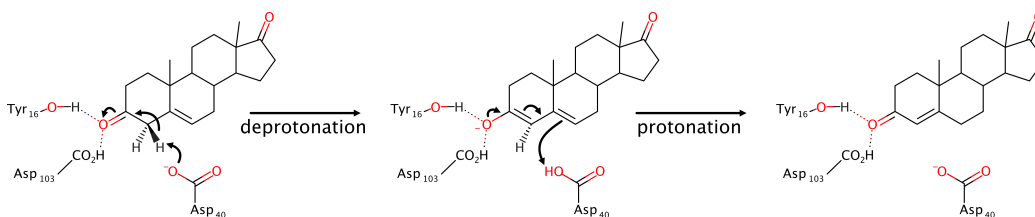
1 Introduction

Enzymes can accelerate chemical reactions by many orders of magnitude. Our understanding of the mechanisms responsible for this process has grown at an increasing rate over the last few decades thanks to two significant advances: i) increasingly accurate structural studies; and ii) improved computational platforms and methods that allows us to predict, among other things, the conformation and energy of folded proteins and the reaction dynamics at enzyme active sites. In addition, these advances generate massive amounts of experimental and theoretical data that has proved effective in the search for statistical correlations to serve as parameters in the predictive models generated with machine learning algorithms. This wealth of data is also useful for identifying new structures and structure-property relationships that may, in turn, be incorporated into the existing chemical formalisms, known collectively as chemical intuition.

Here we demonstrate the applicability of one such structure through an investigation into the causes and effects of electrostatic preorganization [1–4]. Electrostatic preorganization is a strong, non-uniform electric field due to the arrangement and composition of amino acids about the active site, whose specific arrangement is maintained by the larger protein scaffolding. Only recently have accurate assessments of electrostatic preorganization become computationally feasible, with researchers now exploring methods for its analysis, comparison, and interpretation. Meanwhile, the effects of applied electric fields on chemical reactivity have been experimentally and computationally observed for a variety of chemical reactions [5–25], many of which are also catalyzed enzymatically. Hence the specific problem of electrostatic preorganization, and the general problem of electric field catalysis, are of interest to enzymologists. Here we study the model ketosteroid isomerase (KSI) system, the focus of numerous experimental and computational investigations (see Reference 26 for additional references), and build upon previous work elucidating the local structure underlying KSI’s catalytic activity and how that activity can be augmented or hindered [26–28].

The tool used in this investigation, called bond bundle analysis, reduces a system to a set of chemical bonding regions whose energy, extent, electron count, and many other properties can be accurately calculated [29, 30]. In organic systems, understood using valence bond theory, bond bundle analysis often leads to chemically expected conclusions, but with a level of precision and generality not attainable through conventional methods [22, 28, 30].

This two-part investigation proceeds first with a direct inspection of bond bundle property distributions in the KSI active site in the presence and absence of a uniform external electric field (EEF) known to enhance its catalytic activity. In its second part, a set of KSI systems with varying catalytic activity is explored. The investigation reveals the redistribution of electron charge density, $\rho(\mathbf{r})$, between bonds that facilitates the forward reaction direction, and locates the active-site regions that most strongly correspond to catalytic enhancement or inhibition. Significantly, bond bundle analysis allows us to frame our finding within the language and concepts of chemical bonding. This framing leverages, informs, and quantifies many traditionally qualitative chemical concepts. It is this capability that makes bond bundle analysis a promising part of the chemist’s tool kit.



Scheme 1: Steroid isomerization reaction catalyzed by KSI.

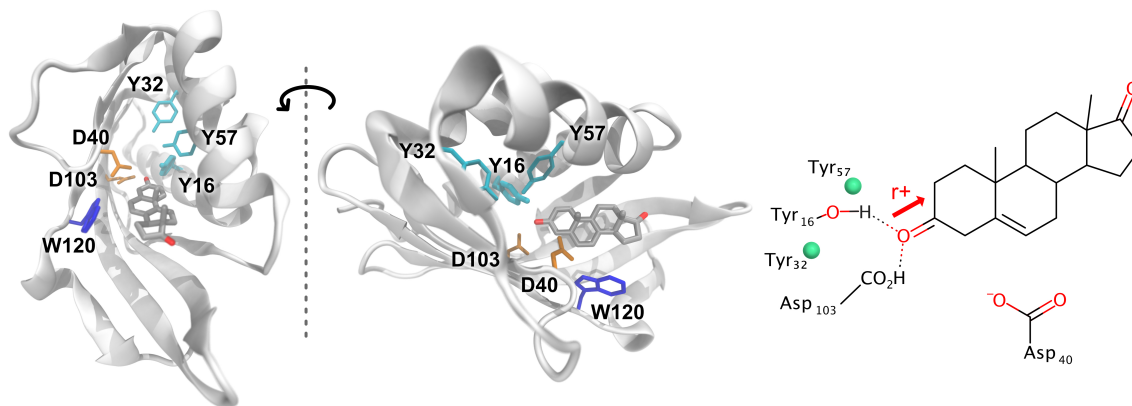


Figure 1: The full KSI protein (PDB code 1O10 [35]) with docked steroid substrate shown from two angles. The tyrosine (Y or Tyr; cyan), aspartic acid (D or Asp; orange) and tryptophan (W or Trp; blue) residues included in the small scale calculation are shown relative to the substrate (colored by element). The Lewis diagram of the system is shown with the “locations” of the 3-chlorotyrosine for the KSI variant systems (Trp₁₂₀ not shown).

2 Background

2.1 Ketosteroid isomerase

The well-studied steroid isomerization reaction that KSI catalyzes involves the repositioning of a double C=C bond in the steroid substrate [26, 27, 31–34]. As shown in Scheme 1, this occurs by the removal of a proton from the secondary β -carbon, which is redeposited at the adjacent secondary carbon. Focusing on the first step, deprotonation is typically pictured as the result of a shift of charge through the substrate π system from the β -carbon to the carbonyl oxygen. In KSI this concerted atomic and electronic rearrangement is facilitated by the ideal positioning of Asp₄₀, providing a general base to receive the proton, and by the oxyanion hole that activates the carbonyl and stabilizes the charged enolate intermediate state.

Fuller *et al.* investigated the effects of applied EEFs to this process using the small-scale KSI active site shown in Figure 1, and found that a field applied parallel to the substrate carbonyl

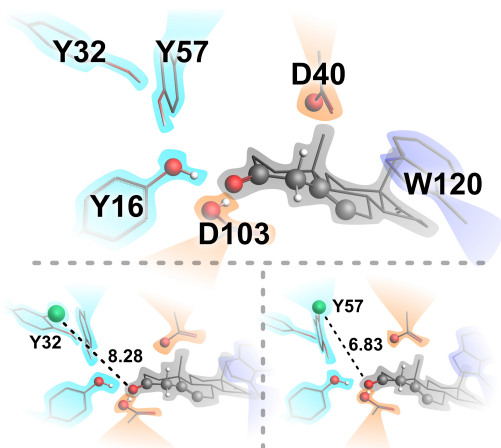


Figure 2: Closer depiction of the arrangement of amino acids forming the “oxyanion hole” about the substrate in KSI (top) and the positioning of the 3-chlorotyrosines in the KSI mutants (bottom) with Cl \cdots O1 distance (Å) indicated.

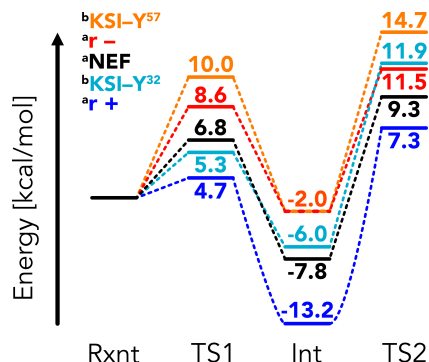


Figure 3: Reaction profiles for the systems in this study. Ordering at top-left is the same as in the TS1 column. ^aData for the NEF and EEF systems taken from Fuller *et al.* [27]. ^bData for KSI-Y systems taken from Hennefarth and Alexandrova [26].

50 bond, pointing from O to C, augmented the electrostatic preorganization, lowering the reaction
 barrier, while a field in the opposite direction had the opposite effect [27]. This agrees with classical
 52 intuition, that an EEF should push charge opposite the field direction, in this case combining
 constructively with the KSI oxyanion hole to more readily shift charge to the carbonyl oxygen—
 54 further stabilizing the enolate intermediate state—and away from the β carbon, increasing its acidity
 and thus facilitating deprotonation.

56 Hennefarth and Alexandrova were then able to show similar reaction barrier effects in KSI vari-
 ants that had a tyrosine mutated to a 3-chlorotyrosine [26]. Because the tyrosines of interest are
 58 involved in the extended hydrogen bonding network around the oxyanion hole (see Figure 2)[36],
 this affects carbonyl activation, altering electrostatic preorganization. They found that a mutated
 60 Tyr₃₂ lowered the barrier, and a mutated Tyr₅₇ raised the barrier relative to the wild type enzyme.

The present investigation uses the small-scale KSI active site, EEF directions, and 3-chlorotyrosine
 62 KSI variants from References 26 and 27 as the starting point for our calculations, and we explicitly
 use the same calculated reaction barrier energies. The five systems: wild type (WT) KSI (a.k.a.
 64 NEF: no electric field), KSI⁺, KSI⁻, KSI-Y³² and KSI-Y⁵⁷ provide a minimum example set of KSI en-
 hancement and inhibition via global and local perturbations; oriented EEFs and amino acid atomic
 66 addition respectively. The regional changes in charge density and energy underlying the reaction

barrier shifts should be accessible using this limited sample.

2.2 Assessing the local charge density origins of KSI catalytic enhancement

A common approach in the search for *local* relationships between $\rho(\mathbf{r})$ and energy related catalytic properties (reaction barriers) is to seek correlations between the property of interest and charge density metrics at points, along one-dimensional paths, or within arbitrarily defined volumes. This approach has been employed to better understand the enhancement and inhibition mechanisms of KSI [26, 27].

Fuller *et al.* checked for correlations between KSI-catalyzed reaction barrier shifts due to EEFs and a number of local properties, such as interatomic distances and values of $\rho(\mathbf{r})$ at bond critical points (CPs) [27]. The strongest correlation found was that of the O2–H1 bond length,¹ which correlated positively with the change in reaction barrier, while the value of $\rho(\mathbf{r})$ at the corresponding bond CP anti-correlated, indicating that direct facilitation of the deprotonation step affects the barrier energy shift. A weaker positive correlation was found with the O1–H2 bond length, indicating, as anticipated, that activation of the carbonyl bond—by decreasing the Asp₄₀–substrate distance—also lowers the reaction barrier.

Given the catalytic role of electrostatics in KSI, Hennefarth and Alexandrova investigated the electric field itself, $\mathbf{E}(\mathbf{r})$, in the KSI active site using both point and regional properties [26]. Here, the set of systems included those exposed to oriented EEFs, and also two 3-chlorotyrosine KSI mutants with respectively higher and lower catalytic activity than WT KSI. They found that the electric field magnitude, $|\mathbf{E}(\mathbf{r})|$, at the O2–H1, C2–H1, and C1=O1 bond CPs correlated strongly with the change in reaction barrier, but only for WT KSI structures; KSI-Y³² and KSI-Y⁵⁷ were outliers to this trend. We take these observations to indicate that the mechanism, through $\rho(\mathbf{r})$, by which the KSI mutants enhance/hinder catalysis may be different than that due to EEFs. Furthermore, the correlation at the carbonyl bond CP showed a nearly constant relationship between $|\mathbf{E}(\mathbf{r})|$ and reaction barrier energy.

Hennefarth and Alexandrova also conducted a regional electric field curvature analysis within two separate rectilinear volumes, one containing the carbonyl C1=O1 atoms, and the other containing the C2–H1...O2 atoms of the reaction site. By evaluating the total curvature along $\mathbf{E}(\mathbf{r})$ streamlines

¹Using the atomic numbering in the present manuscript

96 within each volume, they generated histograms that reflect the relative occupations of high and low
curvature regions—a regional $\mathbf{E}(\mathbf{r})$ fingerprint. The corresponding volumes of multiple systems
98 could then be compared by computing the corresponding histogram distances, thus providing a
scalar similarity metric also useful for statistical evaluation.

100 Using this similarity metric, Hennefarth and Alexandrova found that the $\mathbf{E}(\mathbf{r})$ curvature about
the carbonyl bond had a stronger correlation with reaction barrier than that of the reaction site, with
102 3-chlorotyrosine mutants included in the analysis. This result is counter to the results from point
properties (and those of Fuller *et al.*) that the strongest correlations occur in the reaction site rather
104 than within the substrate. The regional results indicate that activation of the carbonyl enhances
the reaction rate, where point-based analysis results emphasize changes at the deprotonation site.
106 That is, a regional approach seems to better reveal the underlying chemistry at work common to
both the EEF and mutant KSI systems [4, 37].

2.3 The chemical bonding structure of the charge density

Correlations between energy related properties and local charge density metrics abound. However, the assumptions that such relationships exist, and if they do that they are broadly applicable, is questionable, as the local energy of points, lines or arbitrary volumes are all ill defined. Our approach minimizes this concern by building on the Quantum Theory of Atoms in Molecules (QTAIM) and considering only volumes over which energy is well-defined [38, 39].

In its standard form, QTAIM is used to locate the boundaries of the “atoms in molecules,” aka atomic basins. In addition to possessing unambiguous energies, volumes, and charges, these atoms may be characterized by their topology, which, in turn, is described by zero-, one-, and two-dimensional topological $\rho(\mathbf{r})$ features including: critical points designated as nuclear, bond, ring, or cage type; bond paths; and inter-atomic surfaces respectively.

That atomic basins have a well-defined energy results from their satisfaction of a zero flux (of the charge density gradient) boundary condition. For an arbitrary region in $\rho(\mathbf{r})$, one may calculate the average regional kinetic energy using the gradient or Laplacian forms of the quantum mechanical kinetic energy operator, but these values will not match one another. Over a region bounded by zero-flux surfaces, however, these values will agree, and hence the regional energy of an atomic basin is unambiguous [38].

Bond bundle analysis is an extension of QTAIM that recognizes a further partitioning of atomic basins into the smallest regions bounded by zero-flux surfaces called differential gradient bundles (*dGBs*) [40, 41]. To each *dGB* there corresponds an unambiguous energy, and an atomic basin can be decomposed into *dGBs* to produce a continuous and “well-defined energy space.” The topology of this space reveals precise boundaries between intra-atomic regions of charge accumulation called bond wedges. Bond wedges of adjacent atoms then combine to form bond bundles [30, 42].

Figure 4 illustrates the eight atomic basins and seven bond bundles considered in this study, as well as the bond and ring CPs that lie along or interior to their boundaries. See Figure 1.1.3 in the

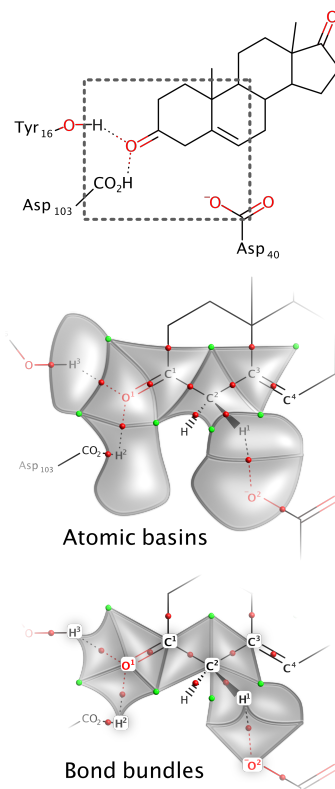


Figure 4: Cartoon depictions of the atomic basins and bond bundles analyzed in this study. Red and green spheres represent bond and ring CPs respectively.

138 supplemental information for a more realistic, three-dimensional representation of bond bundles.
We will appeal to this sort of abstract representation of bond bundles for the remainder of this
140 manuscript. Each has a set of properties commonly associated with a chemical bond, such as an
energy and a number of electrons, which, when taken over all bonds in a system, recover the system
142 energy and electron count. In addition to these common bond-like properties, geometry related
properties may be determined for a bond wedge including: its volume, its normalized solid angle,
144 its total (or average) geometric curvature, and its total (or average) geometric torsion. Section 3 of
the supplemental information includes these and other properties for bond wedges, bond bundles,
146 and atomic basins. Like atomic basins, bond bundles have precise, non-overlapping boundaries that
combine to fill all space.

148 From the wealth of computable gradient bundle properties, we will include in our analysis the
bond wedge solid angle (α), which is the percent area of the nucleus-centered reference sphere
150 occupied by a bond wedge. For example, in a methane molecule, each bond wedge on the sp^3 C
atom would have a solid angle of $\frac{1}{4}$. More typically, these values are not perfectly equal, such as
152 for the sp^2 C3 atom from this study, which, in the WT KSI system, has bond wedge solid angles
of 0.28, 0.30, and 0.43 (from Section 3.1 in the supplemental information). As a system changes,
154 the zero-flux surfaces separating bond wedges move, and their motion carries energetic significance
[43]. Bond wedge surface motion close to the nucleus can be different from the motion far from the
156 nucleus. Bond wedge solid angle indicates atomic division into bond wedges *close to the nucleus*,
as opposed to bond wedge volume, which (when normalized over atomic volume) describes how
158 the entire atomic space is divided into bond wedges. For example, a decrease in bond wedge solid
angle accompanied by an increase in its share of atomic volume would indicate that the bond wedge
160 surfaces contracted close to the nucleus and expanded far from the nucleus.

3 Results and discussion

162 3.1 KSI charge density response to a catalyzing EEF

To illustrate the concrete nature of gradient bundle properties, we begin by inspecting $\rho(\mathbf{r})$ redistri-
164 bution in the KSI active site due to a catalyzing uniform EEF of magnitude $10^{MV/cm}$. Table 1 contains
regional electron counts for atomic basins, bond bundles, and bond wedges in the KSI active site, as

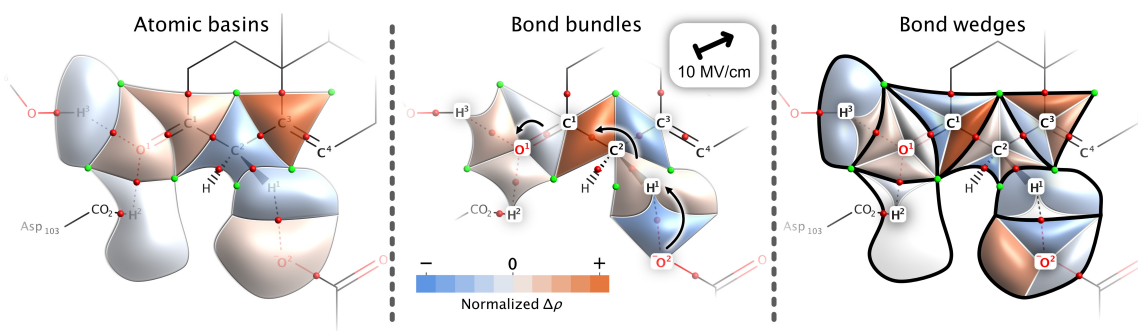


Figure 5: The atomic basins, bond bundles, and bond wedges of KSI (left, middle, and right respectively) shaded according to the changes in their regional electron count due to a 10 MV/cm oriented EEF (the $r+$ direction), which are listed in Table 1. The center image includes the electron-pushing arrows of the deprotonation reaction step.

166 well as their change due to the catalyzing $r+$ EEF. These regional property changes are graphically
 168 depicted in Figure 5, where regions are shaded orange or blue to indicate EEF-induced $\rho(\mathbf{r})$ accu-
 170 mulation or depletion respectively. See Section 3 in the supplemental information for similar tables
 172 for all five systems, for ten different regional properties.

170 The KSI active site response to the EEF is nonuniform, and the bond bundle perspective of this
 172 response simplifies its interpretation. The field activates the carbonyl bond, but its primary effect
 174 is to redistribute charge consistent with the assumed reaction mechanism. Carbonyl activation is
 176 evidenced by the accumulation of charge in the O1 atomic basin (Figure 5; left). However, the
 178 charge redistribution *within* the atomic basin is more informative. The center frame of Figure 5
 180 reveals charge accumulation in the O1 \cdots H2 and O1 \cdots H3 bond bundles as a consequence of charge
 depletion in the O1=C1 bond bundle. Still more pronounced is the charge redistribution occurring
 at the other end of the conjugated system, interior to the substrate. The C1–C2 bond bundle, which
 is believed to increase its bond order from single to double in the deprotonation step, accumulates
 nearly 0.09 electrons in response to the field, offset by decreases in the carbonyl bond and more so
 in the C2–C3 bond.

At the reaction site, the C2–H1 bond, which is broken in the deprotonation step, accumulates
 182 charge due to the EEF, while the incipient O2 \cdots H1 bond loses charge, seemingly the reverse of the
 184 anticipated electron motion. Inspection of the corresponding bond wedge values (Figure 5; right),
 186 however, reveals the expected behavior. The increase in the C2–H1 bond bundle electron count is
 due to the contribution of the C2 atom. The H1 bond wedge component of the C2–H1 bond decreases
 by 0.018 electrons. Because the H1 atom’s other bond wedge, corresponding to the O2 \cdots H1 bond,

Table 1: Regional electron counts in the KSI active site with (EEF) and without (NEF) an applied external electric field of $10^{\text{MV}}/\text{cm}$ pointing from the O nuclear position to the C; the r+ direction. Unnumbered atoms were not included in the study. All regions are truncated at the $\rho = 0.001$ isosurface. Complete gradient bundle integration tables are available in the SI, Section 3.

Atomic basin decomposition	Electron count (ρ) [e]			
	NEF	EEF	Δ	% Δ
C1	5.151	5.185	0.035	0.67
C2	6.207	6.187	-0.021	-0.33
C3	6.182	6.255	0.073	1.18
H1	0.862	0.846	-0.017	-1.92
H2	0.370	0.369	-0.001	-0.22
H3	0.380	0.367	-0.013	-3.46
O1	9.245	9.258	0.013	0.14
O2	9.324	9.329	0.005	0.05
Total	37.721	37.795	0.074	0.20
Bond bundle decomposition	NEF	EEF	Δ	% Δ
C1 — C bond wedge	2.049	2.010	-0.040	-1.93
C1 — C2 bond bundle	3.435	3.524	0.089	2.58
\hookrightarrow C1 bond wedge	2.073	2.157	0.084	4.07
\hookrightarrow C2 bond wedge	1.363	1.367	0.004	0.31
C1 — O1 bond bundle	3.362	3.353	-0.009	-0.28
\hookrightarrow C1 bond wedge	1.029	1.019	-0.010	-0.99
\hookrightarrow O1 bond wedge	2.334	2.334	0.001	0.04
C2 — H bond wedge	1.625	1.574	-0.051	-3.16
C2 — C3 bond bundle	3.214	3.171	-0.042	-1.31
\hookrightarrow C2 bond wedge	1.567	1.563	-0.004	-0.25
\hookrightarrow C3 bond wedge	1.647	1.609	-0.038	-2.32
C2 — H1 bond bundle	2.465	2.478	0.013	0.52
\hookrightarrow C2 bond wedge	1.652	1.683	0.030	1.84
\hookrightarrow H1 bond wedge	0.813	0.795	-0.018	-2.17
C3 — C bond wedge	1.769	1.842	0.073	4.15
C3 — C bond wedge	2.766	2.804	0.038	1.37
H1 — O2 bond bundle	3.662	3.617	-0.046	-1.25
\hookrightarrow H1 bond wedge	0.049	0.050	0.001	2.15
\hookrightarrow O2 bond wedge	3.613	3.566	-0.047	-1.30
H2 — Asp ₁₀₃ bond wedge	0.335	0.335	0.000	0.12
H2 — O1 bond bundle	3.539	3.543	0.005	0.13
\hookrightarrow H2 bond wedge	0.035	0.034	-0.001	-3.46
\hookrightarrow O1 bond wedge	3.503	3.509	0.006	0.17
H3 — Tyr ₁₆ bond wedge	0.321	0.300	-0.022	-6.77
H3 — O1 bond bundle	3.467	3.482	0.014	0.42
\hookrightarrow H3 bond wedge	0.059	0.067	0.009	14.66
\hookrightarrow O1 bond wedge	3.408	3.414	0.006	0.17
O2 — Asp ₄₀ bond wedge	2.114	2.109	-0.005	-0.24
O2 lone pair wedge	3.597	3.654	0.057	1.58
Total	37.721	37.795	0.074	0.20

only increases by 0.001 electrons, we conclude that the remaining 0.017 electrons—the amount lost
188 by the H1 atomic basin—is transferred to the C2 atom rather than redistributed within the H1
atom. That is, shared charge density in the C2–H1 bond was lost by the H1 atom, responsible for at
190 least half of the charge density gained in the corresponding C2 bond wedge. Furthermore, given the
much lower electron counts of the O-bonded H atoms—around $0.37e$ in this case—we posit that the
192 H1 atom, at $0.86e$, loses roughly half an electron during its abstraction to Asp₄₀. The EEF-induced
decrease of $0.017e$ constitutes around 4% of the necessary H1 atomic charge depletion as dictated
194 by the reaction, so here too the $\rho(\mathbf{r})$ response to the EEF appears to facilitate deprotonation.

We have assumed in this discussion that electron charge redistribution primarily occurs between
196 adjacent gradient bundles, however $\rho(\mathbf{r})$ distorts globally in response to any perturbation, and the
direction of charge redistribution is fundamentally nebulous. The “nearsighted” nature of $\rho(\mathbf{r})$ [44–
198 46]—that underlies local chemical functionality and electron-pushing formalisms—here too serves as
a rationale for presuming charge redistribution between adjacent regions. Note that gradient bundle
200 electron count (and other property) changes result from the movement of their bounding surfaces
as well as from the charge redistribution that moves them.

The electron motion determined via gradient bundle analysis recovers and quantifies the tradi-
202 tionally assumed electron motion in unprecedented detail. Still, we note that atomic basins and bond
bundles are merely different unions of bond wedges, each providing its own chemical perspective.
204 By construction, changes to bond wedge $\rho(\mathbf{r})$ must combine to give the atomic basin or bond bundle
changes. Yet owing to their distinct underlying language and associated concepts and models, a very
206 different interpretative process unfolds depending on which is taken to be the irreducible building
208 block of charge density.

3.2 KSI catalytic enhancement and inhibition

210 While the direct inspection of regional properties can be useful for comparison between small numbers
of systems, as above, it can become convoluted with larger datasets or multiple perturbations. As
212 in References 26 and 27, we next take a statistical approach, checking for correlations between the
property of interest (system energy in this case) and regional properties across the five systems: wild
214 type KSI (a.k.a. NEF), EEF-enhanced KSI⁺, EEF-inhibited KSI⁻, enhanced mutant KSI-Y³² and
inhibited mutant KSI-Y⁵⁷.

216 Figure 6 shows a selection of some of the fits of reaction barrier height as a function of different

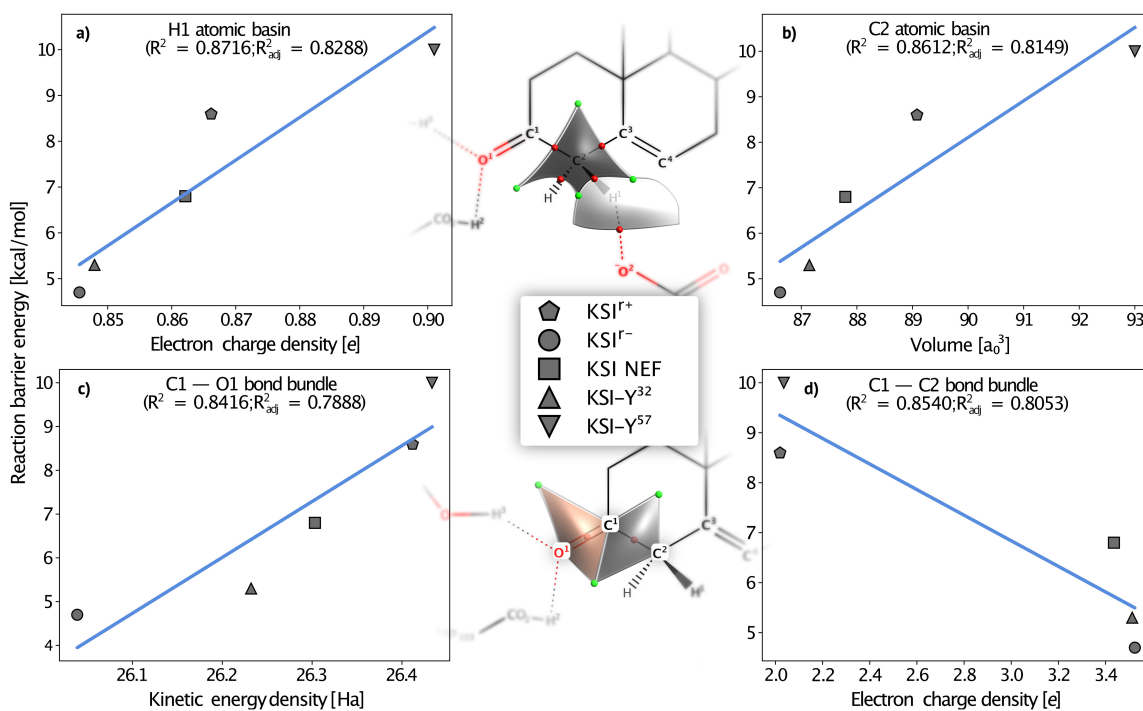


Figure 6: Sampling of atomic basin and bond bundle properties correlated against KSI-catalyzed deprotonation reaction barrier energy. Center: Schematic representation of the atomic basins (top) and bond bundles (bottom) shown. Sides: Plots of regional properties vs barrier energy. Full sets of plots used to generate correlations presented in this manuscript are available in the SI, Section 6.

gradient bundle condensed properties (see Section 6 in the supplemental information for the complete
218 set of plots for all systems). Atomic basin correlations were strongest for the C2 and H1 atoms.
Specifically, the electronic population of the H1 atom correlates positively with reaction barrier,
220 as does the atomic volume of C2. The bond bundle picture, however, indicates that property
shifts within the substrate play an important role, as chemically anticipated. In this case, positive
222 correlation of the O1=C1 bond kinetic energy and negative correlation of the C1–C2 bond population
together indicate that, to lower the reaction barrier, charge should increase in the C1–C2 bond, and
224 kinetic energy should decrease in the O1=C1 bond (thus increasing total energy, weakening the
carbonyl bond), in agreement with results in the previous section.

226 As there are a number of regional properties that can be calculated for bond bundles, bond
wedges, and atomic basins, it is helpful to simplify and plot multiple correlation coefficients simulta-
228 neously, to see at once how *e.g.* volume and energy each correlate, and to access a more immediate
chemical interpretation. Inspired graphically by Reference 47, we have included correlations of re-
230 gional $\rho(\mathbf{r})$ along with regional volume (V), kinetic energy (T), and solid angle (α ; Section 2.3)
as bar charts in Figure 7. Regions are sorted according to the reaction barrier correlations of ρ ,
232 which is also used to shade representative regions as in Figure 5. Note that the shading has opposite
meaning between the two figures, in regards to energetic significance. In Figure 7 a blue-shaded
234 region anti-correlates with reaction barrier energy, so an increase in regional properties should lower
the reaction barrier. Unlike in Figure 5, where an orange region was one in which $\rho(\mathbf{r})$ increased in
236 response to a catalyzing EEF.

In this case, the rate enhancement of the reaction in the KSI active site, resulting from applied
238 electric fields or active-site atomic addition, is achieved by redistributing charge density between
bond bundles in a way that, again, closely resembles our mechanistic understanding of the reac-
240 tion. Specifically, the C1–C2 bond most anti-correlates with reaction barrier energy, indicating that
promoting (or hindering) its transition from single to double bond generally lowers (or raises) the
242 reaction barrier. The O1=C1 and O1 \cdots H3 bond bundles respectively correlate and anti-correlate
with barrier height, indicating that activation of the carbonyl bond—by increasing the O1 atom lone
244 pair density and decreasing the carbonyl bond density—lowers the barrier. At the deprotonation
site, the C2–H1 bond properties anti-correlate with barrier height, paradoxically suggesting that the
246 electron count (and other properties) of the breaking bond should increase rather than decrease.
Altogether, the bond bundle property correlations seem to indicate the same underlying catalytic

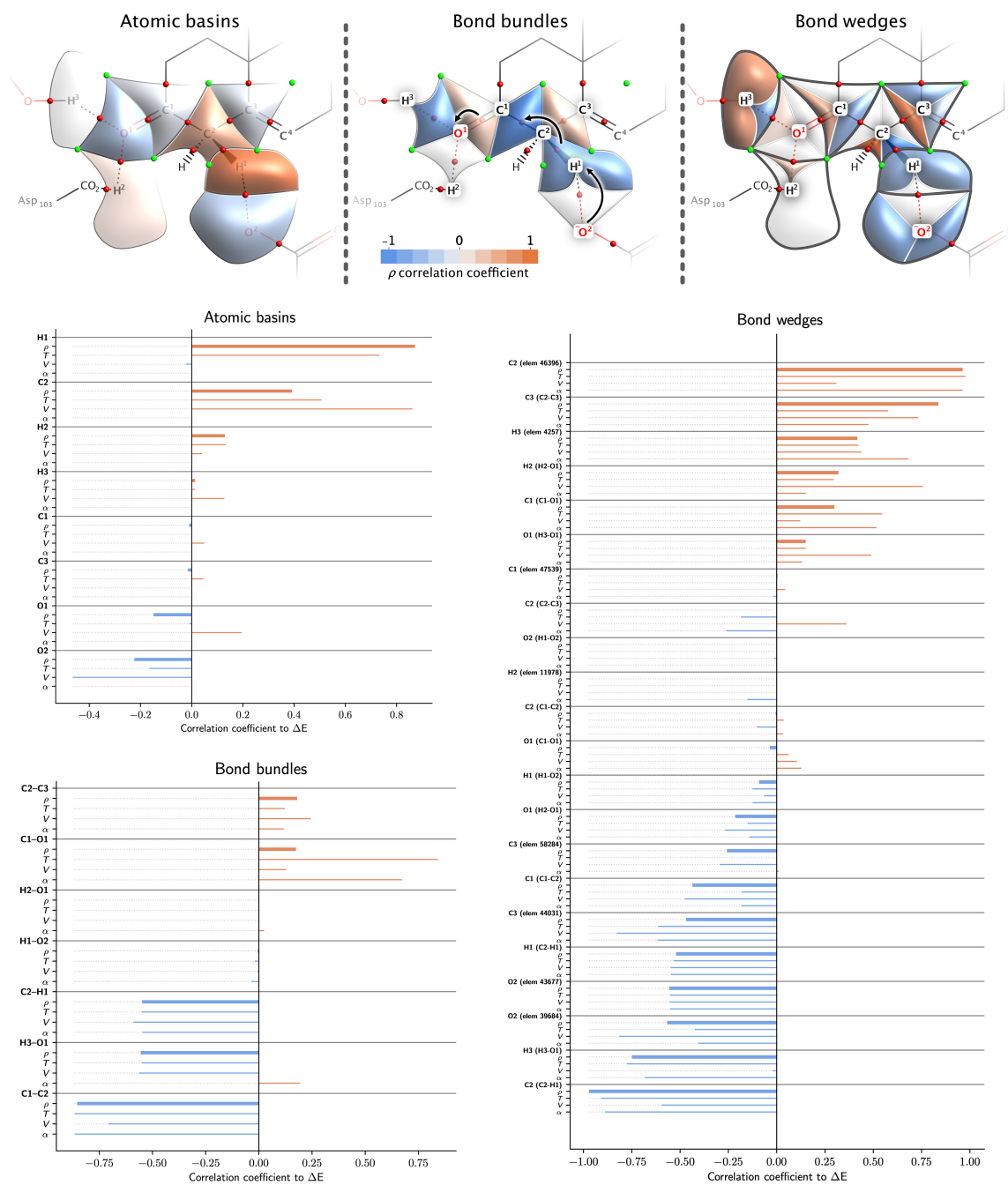


Figure 7: Atomic basin, bond bundle, and bond wedge (top; left to right) property correlations with reaction barrier energy, signed as positive or negative to indicate correlation and anti-correlation. Above are cartoon, schematic depictions of the overlaid on the Lewis representation of the active site, with electron pushing arrows in the center pane denoting the deprotonation reaction step from Scheme 1. Regions are shaded above, and sorted in the plots below, according to the sign and magnitude of their electron population (ρ) correlations with reaction barrier. The regional kinetic energy (T), volume (V), and normalized solid angle (α) are plotted as well. Complete multi-variable correlation bar charts are available in the SI, Section 4.

248 charge density shifts as those resulting from an applied EEF, including the reversed behavior at the
deprotonation site. Here the results indicate a structure property relationship between reactant state
250 substrate bond bundle properties and the barrier height of the KSI-catalyzed reaction, regardless of
the source of bond bundle property perturbation.

252 Another conclusion, similar in part to the previous section, can be arrived at from the inspection
of atomic basin correlations. In this case, the C2 and H1 atoms at the deprotonation site correlate
254 with barrier height, indicating their combined atomic electron count should be lowered—as resulted
from the applied r+ field—in order to facilitate deprotonation. The O1 atom anti-correlates, sug-
256 gesting again that it should be activated via accumulating charge density, but only slightly. However,
while the conjugated carbon system experienced the greatest amount of inter-atomic $\rho(\mathbf{r})$ redistri-
258 bution due to the EEF (Figure 5), the C1 and C3 atomic properties show almost no correlation with
reaction barrier. Instead, the H1 and C2 atoms most strongly correlate. This disparity suggests that
260 the atomic basin $\rho(\mathbf{r})$ redistribution accompanying the catalytic r+ EEF is not generally indicative
of a catalytic effect, but specifically one induced by an EEF. On the other hand, the r+ EEF-induced
262 bond bundle redistribution seems quite indicative of the general behavior shown in Figure 7.

Indeed, the (anti)similarity between bond bundle correlations and EEF-induced bond bundle
264 property shifts is stark. With very few exceptions, regions of $\rho(\mathbf{r})$ accumulation due to the r+ field
(Figure 5) are those that anti-correlate with reaction barrier (Figure 7). Likewise, regions of $\rho(\mathbf{r})$
266 depletion due to the field correlate positively with reaction barrier. Additionally, the C1–C2 bond
bundle, which experienced the greatest increase in $\rho(\mathbf{r})$ due to the EEF, strongly anti-correlates with
268 barrier height. Given that the r+ system was included in the regional correlations, and that it is
the most rate-enhancing system in the (small) sample, it is no surprise that it should be represented
270 in the resulting correlations. However, as noted above, atomic basin regional correlations share less
similarity with their r+ field-induced redistribution in KSI.

272 Regarding the observation that the H1 and C2 atomic basins most strongly correlate with reaction
barrier energy, and how it relates to the underlying mechanism of KSI catalysis. In general, the
274 catalytic effect of an oriented EEF depends on the magnitude of the field, its angle relative to the
dipole of the reaction coordinate (*e.g.* parallel to a bond that is broken or formed in the reaction),
276 and the magnitude of that dipole [5–9, 12, 16–20, 24, 48]. The local electrostatic preorganization
in KSI most underlying its catalytic proficiency is that within the oxyanion hole, which is aligned
278 along the substrate carbonyl bond (the r+ direction)[33, 48]. One might ask how nature determined

that the best way to achieve this atomic basin redistribution is via a carbonyl-oriented field, rather
280 than a field oriented along the reaction coordinate (C2–H1 bond). We previously observed that
a catalyzing EEF, applied to a simple Diels-Alder reaction *along the reaction coordinate*, primarily
282 shifted electron density *within* rather than *between* reactant molecules [22]. Here too the we observe,
in Figure 5, that the r+ field causes bond bundle redistribution *within* the substrate molecule through
284 its conjugated carbon system, and that this results in the same H1 and C2 atomic basin electron
count changes that most correlate with reaction barrier energy. Additionally, the carbonyl is a
286 better candidate for electric field-induced transition state stabilization because its dipole is strong
and does not reorient during the reaction, while the reaction coordinate dipole is weak and does
288 reorient. Thus the carbonyl provides a better EEF “grip” on the molecule, and more “leverage” for
inducing intra-molecular redistribution of charge and other properties.

290 A final and somewhat unexpected similarity to the results of the previous section is the additivity
of bond wedge property correlations to predict those of bond bundles and atomic basins. For
292 example, the two H3 bond wedges strongly correlate and anti-correlate respectively, and the H3
atomic basin as a whole has nearly zero correlation, as if its bond wedges combined to give the
294 whole. The same behavior is apparent in the C1 and C3 atoms, while the H1 atom is clearly an
outlier to this trend. Bond wedge correlations combine to predict those of bond bundles in a similar
296 way, and in this case without exception; the correlation of each bond bundle appears to be the
sum of its bond wedge correlations. While gradient bundle properties are definitionally additive, it
298 cannot be said that gradient bundle energetic significance is additive, in this case in relation to the
catalyzed reaction barrier. Here we have the H1 atom—whose bond wedge correlations would sum
300 to negative rather than positive atomic basin correlation—as our proof by contradiction *against* such
additivity in general. Regardless, bond wedge regional energetic significance does seem to typically
302 combine to predict bond bundle significance.

Regarding the nearly uniform agreement between the correlations of different regional properties
304 with reaction barrier energy, we have previously observed that the regional volume, kinetic energy,
and solid angle tend to correlate strongly with the charge density, at least in organic systems [30].
306 Hence, it is unsurprising that these properties should yield similar correlations with respect to
reaction barrier height, as is clearly the general case in KSI. However, there are exceptions. For
308 example, within the C1–O1 bond bundle in Figure 7, kinetic energy (T) and solid angle (α) correlate
more strongly with reaction barrier ($R^2 \approx 0.7$) than do charge density (ρ) and volume (V) ($R^2 \approx 0.2$).

310 Disagreements of this type indicate weak correlation between the properties, in this case indicating
that within the C1–O1 bond bundle, T and α do not correlate with ρ and V . This assertion is
312 confirmed by inspecting the correlations among regional properties shown in Figure 8. Within the
C1–O1 bond bundle (matrix in center column, bottom row), ρ and V correlate strongly with each
314 other but weakly with T and α , and the reverse is true; T and α correlate strongly with each
other but weakly with ρ and V . The connection between regional property correlation and reaction
316 barrier height correlation is observable for all regions in the study, and similar plots with the full set
of gradient bundle properties, for all gradient bundles, are available in Section 8 of the supplemental
318 information. Within the C1–C2 bond bundle, for example, all four properties strongly anti-correlate
to reaction barrier height (Figure 7; $R^2 \approx 0.8$), and in Figure 8 we see they all strongly correlate
320 with each other as well. Next, the H1 atomic basin has strong ρ and T barrier correlation ($R^2 \approx 0.8$)
but weak V anti-correlation ($R^2 \approx 0.02$), and indeed ρ and T correlate strongly with each other and
322 weakly with V . The C2 atomic basin is similar in both respects to H1, but less pronounced. Finally,
the two C2–H bond wedges are particularly relevant because they experience the strongest overall
324 correlations to reaction barrier height, and for both V correlates more weakly ($R^2 \approx 0.55, 0.31$) than
 ρ , T , or α ($R^2 \approx 0.89$ to 0.98). Likewise, in both C2–H bond wedges, ρ , T , and α correlate strongly
326 with each other and weakly with V .

Because the correlation among regional properties appears to be closely tied to their relative
328 correlations with reaction barrier height, it appears that different types of system changes (*e.g.* an
applied EEF vs. amino acid mutation) enhance catalysis through different mechanisms that affect
330 and utilize some gradient bundle properties more than others. To speculate, this dynamic behavior
is due to constraints imposed by the conserved properties in a chemical process, among them energy,
332 mass (electron count), volume, and gradient bundle solid angle, which are quantified through gradient
bundle analysis. These constraints may operate locally and/or globally. For example, the system
334 electron count may be globally conserved as a whole, but each atomic electron count is also more
or less locally constrained according to its nuclear charge. Gradient bundle solid angle, however,
336 is constrained solely at the atomic level, between the bond wedges of an atom whose solid angles
must sum to unity. As we have seen, these properties tend to correlate, so if a bond electron count
338 increases, so too will its energy (the new electrons possess energy), volume and solid angle (higher
electronic pressure “pushes” out the boundaries of the bond). Although ρ determines the behavior
340 of T , V , and α , each of these properties is individually conserved, which imposes limits on their

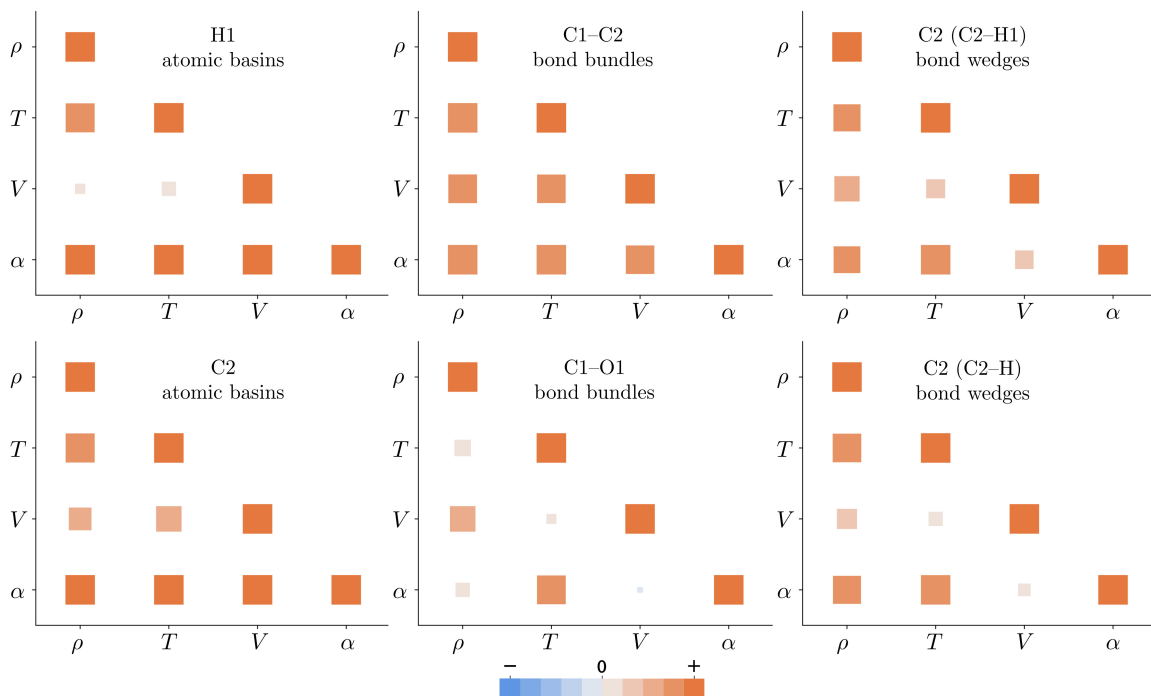


Figure 8: Correlation matrices showing property correlations within a selection of gradient bundles. Electron density (ρ), kinetic energy (T), volume (V), and solid angle (α) are included. For example, the correlation between ρ and α in the H1 atomic basin across all five systems, indicated at the (α, ρ) position in the top-left plot, is stronger than the correlation between ρ and V , which has a smaller, lighter symbol. Full sets of correlation matrices are provided in the SI, Section 8.

ability to vary with respect to ρ . If you add an electron to a bond whose volume is constrained, for example, the electronic pressure will increase. The energy change associated with this will be different than if the bond volume were not constrained. Nature minimizes the energy of the electron density according to the local and global constraints imposed by these conserved gradient bundle properties. A perturbation may also affect some properties more than others. For example, enzyme mutations in the active site directly alter local electron density and atomic/bond volumes, while an applied EEF primarily affects the electron density. Thus gradient bundle properties respond independently, depending on both the type of perturbation and on local property constraints which also vary independently. As demonstrated, gradient bundle analysis captures and contextualizes this intricate property redistribution. We conclude that weak correlation between a region’s properties (*e.g.* the C1–O1 bond bundle, where T and α correlate strongly with each other but weakly with ρ and V) indicates the region is affected by different perturbations in different ways. Conversely, strong correlation between a region’s properties, *together with strong correlation to reaction barrier height* (*e.g.* the C1–C2 bond bundle) indicates that the region has similar energetic significance and catalytic functionality regardless of the type of system change, *i.e.* that it more fundamentally underlies the catalysis. This does not question the link between $|\mathbf{E}(\mathbf{r})|$ at the substrate carbonyl and KSI catalytic activity (see Figure 4d of Reference 48), but does offer a way to qualify and quantify the local regional property changes that underlie this relationship. In future investigations involving larger samples, *e.g.* many mutant and EEF-exposed systems, we can further test this conclusion by performing similar analysis on subsets of the sample, only EEF systems or only mutants, in addition to the full sample.

Overall, in regards to the mechanism of KSI catalytic augmentation, this basic statistical approach leads us to chemically similar conclusions to those of direct inspection of EEF-induced bond bundle property redistributions from the previous section. Activation of the substrate carbonyl bond, and charge accumulation in the C1–C2 bond bundle, as result from the catalyzing r+ EEF, here indicate statistically relevant structure-property relationships between KSI active site gradient bundle properties and reaction barrier height. Correlations of reaction barrier energy to bond bundle regional properties largely recover the expected qualitative electron redistribution of the catalyzed chemical reaction implied through the use of electron-pushing, but in unambiguous, quantitative terms. Surprisingly, we found that bond wedge correlations to reaction barrier energy appear to combine to predict those of bond bundles and atomic basins, that is, typically the statistical rele-

372 vance of bond wedges appears to be additive. Lastly, by extending this analysis to the many com-
putable properties of gradient bundles, we saw that not all properties correlate with reaction barrier
374 to the same degree, and that these differences stem from weak correlation between the regional
properties themselves. This latter observation, we speculate, stems from competing constraints due
376 to the independently conserved properties in a chemical system, and indicates in this case that some
regions respond to applied EEFs different from how they respond to active site amino acid muta-
378 tion. We also expect that this type of statistical approach can be used to investigate reactant state
destabilization in addition to transition state stabilization.

380 4 Conclusion

Here we have presented one method of directly accessing the energies and energy-mediated prop-
382 erties of real-space bonding regions in any chemical system, applied to the specific problem of
KSI catalysis. We inspected the redistribution of $\rho(\mathbf{r})$ due to a catalyzing EEF, qualitatively and
384 quantitatively observed bond transitions similar to those of the conventionally assumed reaction
mechanism, and found that the catalyzing field was that which shifts $\rho(\mathbf{r})$, non-uniformly, in the
386 forward reaction direction. We also found that correlations between reaction barrier energies and
bond bundle properties recovered a similar picture of the expected charge rearrangement.

388 The gradient bundle properties presented here, together with the larger integration tables con-
tained in the supplementary information, are but a small sample of what can currently be calculated.
390 We have only begun to investigate the statistical and conceptual significance of this extensive set
of properties. While we expect direct inspection and graphical depictions to remain useful tools
392 for chemical interpretation, our results demonstrate promise for applications with machine learning
algorithms. A concern with machine learning is that the resulting models may be so abstract as to
394 be unapproachable using physical chemical intuition. Indeed, the more conceptual distance between
the input and output of a machine learning model, the greater the conceptual gap one must span
396 to understand the physical significance of its underlying correlations. To train a model to predict
system energies, and one that can be interpreted in the language of chemistry, it seems doubly ad-
398 vantageous to use input data that explicitly include the precise energy of the bonds in the system.
Thus gradient bundle regional properties show promise for machine learning, for training models
400 such as that of Reference 49.

Constructing a complete, descriptive network of enzyme $\rho(\mathbf{r})$ structure-property relationships, such that local changes in $\rho(\mathbf{r})$ could be used to accurately predict catalytic rate enhancement, will be a formidable task owing to the lack of underlying energetic additivity between the independent properties of enzymes [32]. Bond bundles do possess spatial and energetic additivity, are uniquely defined in any chemical system, and their analysis appears to naturally leverage our hard won understanding of chemical bonding. Furthermore, in this case the correlation of bond wedge properties with rate enhancement did, in fact, appear to be additive, so there is a readily quantifiable sense in which catalyzing features may have underlying energetic additivity. Bond wedge and bond bundles are thus attractive tools for identifying, measuring, and contextualizing $\rho(\mathbf{r})$ and other property redistribution that accompanies and underlies enzymatic catalysis.

Methods

All *ab-initio* calculations were performed using the ADF package of The Amsterdam Modeling Suite [50–52]. Relaxed system geometries were obtained with initial coordinates from References 27 and 26 as mentioned above. Optimization of all five systems was performed using a triple- ζ STO all-electron basis set with one polarization function [53], with the Minnesota’06-2X XC energy density functional [54, 55] and “good” numerical integration quality. The NEF system relaxation also included implicit COSMO solvation [56, 57] using Allinger solvent radii and a dielectric constant of $\epsilon = 4.0$. Subsequent single-point calculations were run with the same basis set and functional, with the same COSMO settings now used for all systems. All applied electric fields were of magnitude $10^{\text{MV/cm}}$. The formaldehyde calculation results in Table 1 used a triple- ζ all-electron basis set with the PBE functional [58].

Topological analysis, along with atomic basin and bond bundle/wedge decomposition was performed with the Bondalyzer software suite of the Molecular Theory Group at Colorado School of Mines [59], an add-on to the Tecplot360 visualization package [60]. Statistical analysis was performed in Python, and the Matplotlib [61] and SeaBorn [62] libraries were used for plotting line/scatter and bar charts respectively. Chemical diagrams were composed in MarvinSketch [63]. Final figures were compiled in Affinity Designer [64].

Acknowledgments

This work was supported by the National Science Foundation grant CHE-1903808, and by the Office of Naval Research grants N00014-05-C-0241 and N00014-10-1-0838.

Supporting information

Supporting information is provided free of charge at (link to SI)

- 3D depictions of some of the regions discussed in the manuscript
- Coordinates and energies of *ab-initio* calculations
- Atomic basin, bond bundle, and bond wedge tabulated integration values *with many more properties than are included in this manuscript*
- Single and multi-variable bar charts of simplified regional property correlations
- Plots of fits of each region and property with reaction barrier energy
- Correlations among regional properties

References

- [1] Arieh Warshel. Electrostatic basis of Structure–Function correlation in proteins. *Accounts of Chemical Research*, 14:284–290, 1981.
- [2] Arieh Warshel. Electrostatic Origin of the Catalytic Power of Enzymes and the Role of Pre-organized Active Sites*. *Journal of Biological Chemistry*, 273(42):27035–27038, October 1998. doi:10.1074/jbc.273.42.27035.
- [3] Arieh Warshel, Pankaz K. Sharma, Mitsunori Kato, Yun Xiang, Hanbin Liu, and Mats H. M. Olsson. Electrostatic Basis for Enzyme Catalysis. *Chemical Reviews*, 106(8):3210–3235, August 2006. doi:10.1021/cr0503106.
- [4] Matthew R. Hennefarth and Anastassia N. Alexandrova. Advances in optimizing enzyme electrostatic preorganization. *Current Opinion in Structural Biology*, 72:1–8, February 2022. doi:10.1016/j.sbi.2021.06.006.

- 452 [5] Rinat Meir, Hui Chen, Wenzhen Lai, and Sason Shaik. Oriented Electric Fields Accelerate
Diels–Alder Reactions and Control the endo/exo Selectivity. *ChemPhysChem*, 11(1):301–310,
454 2010. doi:10.1002/cphc.200900848.
- [6] Albert C. Aragonès, Naomi L. Haworth, Nadim Darwish, Simone Ciampi, Nathaniel J. Bloom-
456 field, Gordon G. Wallace, Ismael Diez-Perez, and Michelle L. Coote. Electrostatic catalysis of
a Diels–Alder reaction. *Nature*, 531(7592):88–91, March 2016. doi:10.1038/nature16989.
- 458 [7] Sason Shaik, Debasish Mandal, and Rajeev Ramanan. Oriented electric fields as future smart
reagents in chemistry. *Nature Chemistry*, 8(12):1091–1098, December 2016. doi:10.1038/
460 nchem.2651.
- [8] Zhanfeng Wang, David Danovich, Rajeev Ramanan, and Sason Shaik. Oriented-External Elec-
462 tric Fields Create Absolute Enantioselectivity in Diels–Alder Reactions: Importance of the
Molecular Dipole Moment. *Journal of the American Chemical Society*, 140(41):13350–13359,
464 October 2018. doi:10.1021/jacs.8b08233.
- [9] Chao Wang, David Danovich, Hui Chen, and Sason Shaik. Oriented External Electric Fields:
466 Tweezers and Catalysts for Reactivity in Halogen-Bond Complexes. *Journal of the American
Chemical Society*, 141(17):7122–7136, May 2019. doi:10.1021/jacs.9b02174.
- 468 [10] Ming-Xia Zhang, Hong-Liang Xu, and Zhong-Min Su. The directions of an external electric
field control the catalysis of the hydroboration of C–O unsaturated compounds. *RSC Advances*,
470 9(50):29331–29336, September 2019. doi:10.1039/C9RA03895G.
- [11] Yaping Zang, Qi Zou, Tianren Fu, Fay Ng, Brandon Fowler, Jingjing Yang, Hexing Li,
472 Michael L. Steigerwald, Colin Nuckolls, and Latha Venkataraman. Directing isomerization
reactions of cumulenes with electric fields. *Nature Communications*, 10(1):4482, October 2019.
474 doi:10.1038/s41467-019-12487-w.
- [12] Edoardo Jun Mattioli, Andrea Bottoni, Francesco Zerbetto, and Matteo Calvaresi. Oriented
476 External Electric Fields Affect Rate and Stereoselectivity of Electrocyclic Reactions. *The Jour-
nal of Physical Chemistry C*, 123(43):26370–26378, October 2019. doi:10.1021/acs.jpcc.
478 9b07358.

- [13] Carles Acosta-Silva, Joan Bertran, Vicenç Branchadell, and Antoni Oliva. Kemp Elimination Reaction Catalyzed by Electric Fields. *ChemPhysChem*, 21(4):295–306, 2020. doi:10.1002/cphc.201901155.
- [14] Thijs Stuyver, David Danovich, Jyothish Joy, and Sason Shaik. External electric field effects on chemical structure and reactivity. *WIREs Computational Molecular Science*, 10(2):e1438, 2020. doi:10.1002/wcms.1438.
- [15] Mark Dittner and Bernd Hartke. Globally optimal catalytic fields for a Diels–Alder reaction. *The Journal of Chemical Physics*, 152(11):114106, March 2020. doi:10.1063/1.5142839.
- [16] Sason Shaik, David Danovich, Jyothish Joy, Zhanfeng Wang, and Thijs Stuyver. Electric-Field Mediated Chemistry: Uncovering and Exploiting the Potential of (Oriented) Electric Fields to Exert Chemical Catalysis and Reaction Control. *Journal of the American Chemical Society*, 142(29):12551–12562, July 2020. doi:10.1021/jacs.0c05128.
- [17] Fengyi Liu and Minjuan Liu. An Intuitive Electric-field Contribution Decomposition Model for Chemical Processes and Its Applications on Diels-Alder Reactions. *Chemical Research in Chinese Universities*, 36(6):1241–1248, December 2020. doi:10.1007/s40242-020-0143-x.
- [18] Song Yu, Pascal Vermeeren, Trevor A. Hamlin, and F. Matthias Bickelhaupt. How Oriented External Electric Fields Modulate Reactivity. *Chemistry – A European Journal*, 27(18):5683–5693, 2021. doi:10.1002/chem.202004906.
- [19] S. Shaik, D. Danovich, K. D. Dubey, and T. Stuyver. The Impact of Electric Fields on Chemical Structure and Reactivity. In *Effects of Electric Fields on Structure and Reactivity*, pages 12–70. The Royal Society of Chemistry, March 2021. doi:10.1039/9781839163043-00012.
- [20] Nadia G. Léonard, Rakia Dhaoui, Teera Chantarojsiri, and Jenny Y. Yang. Electric Fields in Catalysis: From Enzymes to Molecular Catalysts. *ACS Catalysis*, 11(17):10923–10932, September 2021. doi:10.1021/acscatal.1c02084.
- [21] Wei-Wei Wang, Fu-Lin Shang, and Xiang Zhao. Switchable (2 + 2) and (4 + 2) Cycloadditions on Boron Nitride Nanotubes under Oriented External Electric Fields: A Mechanistic Study. *The Journal of Organic Chemistry*, 86(5):3785–3791, March 2021. doi:10.1021/acs.joc.0c02590.

- 506 [22] Timothy Wilson and Mark Eberhart. A Bond Bundle Case Study of Diels-Alder Catalysis Using
Oriented Electric Fields. January 2022. doi:10.26434/chemrxiv-2021-17wpx-v2.
- 508 [23] Valerie Vaissier Welborn, Luis Ruiz Pestana, and Teresa Head-Gordon. Computational opti-
mization of electric fields for better catalysis design. *Nature Catalysis*, 1(9):649–655, September
510 2018. doi:10.1038/s41929-018-0109-2.
- [24] Shahin Sowlati-Hashjin, Mikko Karttunen, and Chérif F. Matta. Manipulation of Diatomic
512 Molecules with Oriented External Electric Fields: Linear Correlations in Atomic Properties
Lead to Nonlinear Molecular Responses. *The Journal of Physical Chemistry A*, 124(23):4720–
514 4731, June 2020. doi:10.1021/acs.jpca.0c02569.
- [25] Daniel Bím and Anastassia N. Alexandrova. Local Electric Fields As a Natural Switch of
516 Heme-Iron Protein Reactivity. *ACS Catalysis*, 11(11):6534–6546, June 2021. doi:10.1021/
acscatal.1c00687.
- 518 [26] Matthew R. Hennefarth and Anastassia N. Alexandrova. Direct Look at the Electric Field in
Ketosteroid Isomerase and Its Variants. *ACS Catalysis*, 10(17):9915–9924, September 2020.
520 doi:10.1021/acscatal.0c02795.
- [27] Jack Fuller, Tim R. Wilson, Mark E. Eberhart, and Anastassia N. Alexandrova. Charge Density
522 in Enzyme Active Site as a Descriptor of Electrostatic Preorganization. *Journal of Chemical
Information and Modeling*, 59(5):2367–2373, May 2019. doi:10.1021/acs.jcim.8b00958.
- 524 [28] Timothy R. Wilson, Anastassia N. Alexandrova, and M. E. Eberhart. Electron Density Geom-
etry and the Quantum Theory of Atoms in Molecules. *The Journal of Physical Chemistry A*,
526 125(50):10622–10631, December 2021. doi:10.1021/acs.jpca.1c09359.
- [29] Travis E Jones and Mark E Eberhart. The Bond Bundle in Open Systems. *International*
528 *Journal of Quantum Chemistry*, 110(8):1500–1505, 2010. doi:10.1002/qua.22270.
- [30] Timothy R. Wilson, Malavikha Rajivmoorthy, Jordan Goss, Sam Riddle, and Mark E. Eber-
530 hart. Observing the 3D Chemical Bond and its Energy Distribution in a Projected Space.
ChemPhysChem, 20(24):3289–3305, 2019. doi:10.1002/cphc.201900962.
- 532 [31] Daniel A. Kraut, Paul A. Sigala, Brandon Pybus, Corey W. Liu, Dagmar Ringe, Gregory A.
Petsko, and Daniel Herschlag. Testing Electrostatic Complementarity in Enzyme Catalysis:

- 534 Hydrogen Bonding in the Ketosteroid Isomerase Oxyanion Hole. *PLOS Biology*, 4(4):e99, March
2006. doi:10.1371/journal.pbio.0040099.
- 536 [32] Daniel Herschlag and Aditya Natarajan. Fundamental Challenges in Mechanistic Enzymol-
ogy: Progress toward Understanding the Rate Enhancements of Enzymes. *Biochemistry*,
538 52(12):2050–2067, March 2013. doi:10.1021/bi4000113.
- [33] Stephen D. Fried, Sayan Bagchi, and Steven G. Boxer. Extreme electric fields power catalysis
540 in the active site of ketosteroid isomerase. *Science*, 346(6216):1510–1514, December 2014.
- [34] Arieh Warshel, Pankaz K. Sharma, Zhen T. Chu, and Johan Åqvist. Electrostatic Contribu-
542 tions to Binding of Transition State Analogues Can Be Very Different from the Corresponding
Contributions to Catalysis: Phenolates Binding to the Oxyanion Hole of Ketosteroid Isomerase.
544 *Biochemistry*, 46(6):1466–1476, February 2007. doi:10.1021/bi061752u.
- [35] Gregory M. Vath, Cathleen A. Earhart, James V. Rago, Michael H. Kim, Gregory A. Bohach,
546 Patrick M. Schlievert, and Douglas H. Ohlendorf. The Structure of the Superantigen Exfoliative
Toxin A Suggests a Novel Regulation as a Serine Protease,. *Biochemistry*, 36(7):1559–1566,
548 February 1997. doi:10.1021/bi962614f.
- [36] Paul A. Sigala, Aaron T. Fafarman, Jason P. Schwans, Stephen D. Fried, Timothy D. Fenn,
550 Jose M. M. Caaveiro, Brandon Pybus, Dagmar Ringe, Gregory A. Petsko, Steven G. Boxer, and
Daniel Herschlag. Quantitative dissection of hydrogen bond-mediated proton transfer in the ke-
552 tosteroid isomerase active site. *Proceedings of the National Academy of Sciences*, 110(28):E2552–
E2561, July 2013. doi:10.1073/pnas.1302191110.
- 554 [37] Matthew R. Hennefarth and Anastassia N. Alexandrova. Heterogeneous Intramolecular Elec-
tric Field as a Descriptor of Diels–Alder Reactivity. *The Journal of Physical Chemistry A*,
556 125(5):1289–1298, February 2021. doi:10.1021/acs.jpca.1c00181.
- [38] R F W Bader, T T Nguyen-Dang, and Per-Olov Löwdin. Quantum Theory of Atoms in
558 Molecules–Dalton Revisited. In *Advances in Quantum Chemistry*, volume Volume 14, pages
63–124. Academic Press, 1981. doi:10.1016/S0065-3276(08)60326-3.
- 560 [39] Chérif F Matta and Russell J Boyd. *The Quantum Theory of Atoms in Molecules: From Solid
State to DNA and Drug Design*. Weinheim: Wiley-VCH, 2007.

- 562 [40] Amanda Morgenstern, Tim Wilson, Jonathan Miorelli, Travis Jones, and M E Eberhart. In
Search of an Intrinsic Chemical Bond. *Computational and Theoretical Chemistry*, 1053(0):31–
564 37, 2015. doi:<http://dx.doi.org/10.1016/j.comptc.2014.10.009>.
- [41] Amanda Morgenstern and Mark Eberhart. Bond dissociation energies from the topology of the
566 charge density using gradient bundle analysis. *Physica Scripta*, 91(2):23012, 2016.
- [42] Timothy R. Wilson and M.E. Eberhart. Quantum theory of atoms in molecules in condensed
568 charge density space. *Canadian Journal of Chemistry*, 97(11):757–762, July 2019. doi:10.
1139/cjc-2019-0086.
- 570 [43] Amanda Morgenstern, Charles Morgenstern, Jonathan Miorelli, Mark E Eberhart, and Tim
Wilson. The Influence of Zero-Flux Surface Motion on Chemical Reactivity. *Physica Scripta*,
572 18(7):5638–5646, January 2016. doi:10.1039/C5CP07852K.
- [44] E. Prodan and W. Kohn. Nearsightedness of electronic matter. *Proceedings of the National
574 Academy of Sciences of the United States of America*, 102(33):11635–11638, 2005.
- [45] E. Prodan. Nearsightedness of electronic matter in one dimension. *Physical Review B*,
576 73(8):085108, February 2006.
- [46] Richard F W Bader. Nearsightedness of electronic matter as seen by a physicist and a chemist.
578 *Journal of Physical Chemistry A*, 112:13717–13728, 2008. doi:10.1021/jp806282j.
- [47] Adriano M. Luchi, Roxana N. Villafañe, J. Leonardo Gómez Chávez, M. Lucrecia Bogado,
580 Emilio L. Angelina, and Nelida M. Peruchena. Combining Charge Density Analysis with
Machine Learning Tools To Investigate the Cruzain Inhibition Mechanism. *ACS Omega*,
582 4(22):19582–19594, November 2019. doi:10.1021/acsomega.9b01934.
- [48] Stephen D. Fried and Steven G. Boxer. Electric Fields and Enzyme Catalysis. *Annual Review
584 of Biochemistry*, 86(1):387–415, June 2017. doi:10.1146/annurev-biochem-061516-044432.
- [49] Santiago Vargas, Matthew R. Hennefarth, Zhihao Liu, and Anastassia N. Alexandrova. Machine
586 Learning to Predict Diels–Alder Reaction Barriers from the Reactant State Electron Density.
Journal of Chemical Theory and Computation, 17(10):6203–6213, October 2021. doi:10.1021/
588 acs.jctc.1c00623.

- [50] G te Velde, F M Bickelhaupt, E J Baerends, C Fonseca Guerra, S J A van Gisbergen, J G Snijders, and T Ziegler. Chemistry with ADF. *Journal of Computational Chemistry*, 22(9):931–967, 2001. doi:10.1002/jcc.1056.
- [51] C. Fonseca Guerra, J. G. Snijders, G. te Velde, and E. J. Baerends. Towards an order-N DFT method. *Theoretical Chemistry Accounts*, 99(6):391–403, November 1998. doi:10.1007/s002140050353.
- [52] ADF 2019.3. SCM, 2019.
- [53] E Van Lenthe and E J Baerends. Optimized Slater-type basis sets for the elements 1–118. *Journal of Computational Chemistry*, 24(9):1142–1156, 2003. doi:10.1002/jcc.10255.
- [54] Yan Zhao and Donald G. Truhlar. A new local density functional for main-group thermochemistry, transition metal bonding, thermochemical kinetics, and noncovalent interactions. *The Journal of Chemical Physics*, 125(19):194101, November 2006. doi:10.1063/1.2370993.
- [55] Yan Zhao and Donald G Truhlar. The M06 suite of density functionals for main group thermochemistry, thermochemical kinetics, noncovalent interactions, excited states, and transition elements: Two new functionals and systematic testing of four M06-class functionals and 12 other function. *Theoretical Chemistry Accounts*, 120(1):215–241, 2008. doi:10.1007/s00214-007-0310-x.
- [56] Andreas Klamt. Conductor-like Screening Model for Real Solvents: A New Approach to the Quantitative Calculation of Solvation Phenomena. *The Journal of Physical Chemistry*, 99(7):2224–2235, February 1995. doi:10.1021/j100007a062.
- [57] Cory C. Pye and Tom Ziegler. An implementation of the conductor-like screening model of solvation within the Amsterdam density functional package. *Theoretical Chemistry Accounts*, 101(6):396–408, May 1999. doi:10.1007/s002140050457.
- [58] John P. Perdew, Kieron Burke, and Matthias Ernzerhof. Generalized Gradient Approximation Made Simple. *Physical Review Letters*, 77(18):3865–3868, October 1996. doi:10.1103/PhysRevLett.77.3865.
- [59] Tim R. Wilson and Mark E. Eberhart. Bondalyzer. First Principles Materials Design and Software, October 2021.

- [60] Tecplot Inc. Tecplot 360 2013R1. Tecplot Inc., 2013.
- 618 [61] J D Hunter. Matplotlib: A 2D graphics environment. *Computing In Science & Engineering*, 9(3):90–95, 2007.
- 620 [62] Michael L. Waskom. Seaborn: Statistical data visualization. *Journal of Open Source Software*, 6(60):3021, 2021. doi:10.21105/joss.03021.
- 622 [63] Marvin — ChemAxon. <https://chemaxon.com/products/marvin>.
- [64] Affinity Designer – Professional Graphic Design Software. [https://affinity.serif.com/en-](https://affinity.serif.com/en-us/designer/)
624 [us/designer/](https://affinity.serif.com/en-us/designer/).